AIAA JOURNAL
Vol. 33, No. 3, March 1995

Turbulence Anisotropy and Near-Wall Modeling in Predicting Three-Dimensional Shear-Flows

F. Sotiropoulos* and V. C. Patel†
University of Iowa, Iowa City, Iowa 52242-1585

Three-dimensional turbulent flow in a circular-to-rectangular transition duct is studied to assess the role of near-wall modeling and turbulence anisotropy in predicting the origin and growth of longitudinal vorticity and the secondary motion with which it is associated. Calculations are carried out using the standard k-ε model and the Reynolds stress transport closure of Gibson and Launder (GL), both of which use wall functions. The computed solutions are compared with experimental data and with calculations previously reported by the authors which employed the near-wall version of the GL model proposed by Launder and Shima (LSH). These comparisons lead to the conclusion that accurate description of most three-dimensional turbulent flows, regardless of their origin, would require turbulence models that 1) resolve the near-wall flow and 2) account for anisotropy of the Reynolds stresses. Further evidence to support the latter conclusion is provided by employing the LSH solution to evaluate the various terms in the mean longitudinal-vorticity equation. It is shown that, vortex stretching, vortex skewing, and generation and destruction of vorticity by Reynolds stresses are all dominant in one region or another.

Introduction

THREE-DIMENSIONAL flows, whether laminar or turbulent, are most often described in terms of primary and secondary velocities, the term primary referring to velocity along the predominant flow (streamwise) direction and secondary to velocity components in planes normal to the primary direction. With few exceptions (massively separated flows, for example), the so-defined secondary velocity components are typically an order of magnitude smaller than the primary velocity. In a recent review of turbulent secondary flows, Bradshaw[1] succinctly summarized the various mechanisms that are involved in the generation of secondary motion but suggested that the review was "as much a list of inadequacies as achievements." This assessment of the state of the art was prompted, no doubt, by the apparent lack of progress in methods for the prediction of such flows.

Secondary motion, by definition, implies the existence of streamwise, or longitudinal, vorticity. The physical mechanisms associated with the origin, growth, and decay of secondary motion, therefore, can be understood by considering the transport equation for longitudinal vorticity, which in Cartesian coordinates reads

$$\underbrace{U\frac{\partial \Omega_x}{\partial x}+V\frac{\partial \Omega_x}{\partial y}+W\frac{\partial \Omega_x}{\partial z}}_{A_1}=\underbrace{\Omega_x\frac{\partial U}{\partial x}}_{A_2}+\underbrace{\Omega_y\frac{\partial U}{\partial y}+\Omega_z\frac{\partial U}{\partial z}}_{A_3}$$

$$+\underbrace{\frac{\partial}{\partial x}\left(\frac{\partial \overline{uv}}{\partial z}-\frac{\partial \overline{uw}}{\partial y}\right)+\left(\frac{\partial^2}{\partial y^2}-\frac{\partial^2}{\partial z^2}\right)(-\overline{vw})+\frac{\partial^2}{\partial y\partial z}\left(\overline{v^2}-\overline{w^2}\right)}_{A_4}$$

$$+\underbrace{\nu\left(\frac{\partial^2}{\partial x^2}+\frac{\partial^2}{\partial y^2}+\frac{\partial^2}{\partial z^2}\right)\Omega_x}_{A_5} \qquad (1)$$

where x is aligned with the streamwise direction, the mean-vorticity components in the (x, y, z) directions are $(\Omega_x, \Omega_y, \Omega_z)$, the mean-velocity components are (U, V, W), the corresponding turbulent fluctuating velocities are (u, v, w), ν is kinematic viscosity, and overbars denote time averages. The group of terms A_1 represents convection of streamwise vorticity by the mean flow. A_2 represents the stretching of longitudinal vorticity in the streamwise direction and responds to the streamwise acceleration or deceleration of the flow. A_3 represents the production of streamwise vorticity by lateral skewing (rotation) of the vorticity vector and is responsible for producing what Prandtl termed "secondary motion of the first kind." Secondary flows in which A_3 is significant are characterized by transverse pressure gradients and, therefore, they are also referred to as pressure-driven secondary motions. All of the given mechanisms are, of course, active even in inviscid, nonturbulent flows. The group of terms A_4, containing the Reynolds stresses, is the distinguishing feature of turbulent flows and represents the production (positive or negative) or diffusion of longitudinal vorticity. Prandtl referred to flows in which this mechanism is dominant as "secondary motion of the second kind." They are also referred to as stress-driven secondary motions. The last set of terms A_5 represents diffusion by viscous action. In turbulent flow, it is generally assumed that this term is small in comparison with A_4 everywhere except in the sublayer next to a solid surface.

In the modeling of three-dimensional turbulent flows there are at least two critical issues that require careful consideration: 1) the level of turbulence closure necessary for successful predictions and 2) the treatment of the near-wall layers. The selection of an appropriate turbulence closure depends on the relative importance of the various mechanisms that contribute to the development and decay of longitudinal vorticity in the flow under consideration. When modeling, for instance, flows through straight noncircular ducts—where Reynolds-stress anisotropy drives the secondary motion—it is generally accepted that the minimum level of turbulence closure should be one that is capable of reproducing the anisotropy of the normal stresses and distributions of the shear stresses.[2] For flows with strong induced pressure gradients, on the other hand, such as flows in curved ducts, pipes, transition ducts, etc., the secondary motion originates via the lateral skewing mechanism (pressure-driven secondary motion). Consequently, it is frequently argued that standard isotropic models should be sufficient for resolving such flows. One may speculate, however, that the Reynolds stress field associated with a strong pressure-driven secondary motion may become significant enough to control the subsequent dynamics of the flow and, in flows such as wakes of three-dimensional bodies, it may be the only mechanism for the decay of longitudinal vorticity. Thus it is important to understand the coupling between the two mechanisms that control the secondary motion and the evolution and

Received March 23, 1994; revision received Aug. 30, 1994; accepted for publication Aug. 31, 1994. Copyright © 1994 by the American Institute of Aeronautics and Astronautics, Inc. All rights reserved.

*Assistant Research Scientist, Iowa Institute of Hydraulic Research and Department of Mechanical Engineering. Member AIAA.

†Professor, Iowa Institute of Hydraulic Research and Department of Mechanical Engineering. Associate Fellow AIAA.

decay of longitudinal vorticity before deciding on the level of turbulence closure required for successful predictions of complex, three-dimensional flows.

Insofar as the treatment of the near-wall flow is concerned, the most popular approach is to utilize the so-called wall-functions, that is, to employ the logarithmic velocity distribution and the local-equilibrium assumptions associated with it to bridge the gap between the fully turbulent region and the laminar sublayer. The validity of this approach, however, is at best questionable in complex, three-dimensional flows since 1) it is based on assumptions which have been validated only in simple two-dimensional boundary-layer flows with small pressure gradients and 2) it avoids the resolution of the all important wall region, where much of the secondary motion originates. Nevertheless, this approach has been extensively used in modeling complex flows, primarily because it is computationally efficient and expedient. The alternative to the wall-functions approach is to employ turbulence closures that are valid all the way to wall. Although several such closures have been proposed in the literature,[3,4] their use in complex flows has been rather limited, mainly due to the substantial numerical difficulties associated with their implementation (requiring very fine computational meshes and involving numerical stiffness of the resulting equations).

The objective of the present paper is to report a systematic study of the role of near-wall modeling and turbulence anisotropy in the origin and growth of longitudinal vorticity in a three-dimensional flow. The flow through the circular-to-rectangular (CR) transition duct of Davis and Gessner,[5] previously calculated by the authors[6] using the near-wall Reynolds stress transport closure of Launder and Shima (LSH),[7] is revisited by carrying out calculations using the standard, isotropic k-ε model and the Reynolds stress transport closure of Gibson and Launder (GL),[8] both with wall functions. The GL closure is selected from several available high Reynolds number second moment closures because its low Reynolds number version, due to Launder and Shima,[7] was very successful in predicting the flow through the CR duct.[6] Thus, comparisons of the GL and LSH predictions enable assessment of the wall-functions approach in three-dimensional flows. Comparisons of the k-ε and GL predictions, on the other hand, clarify the role of turbulence anisotropy. To eliminate numerical uncertainties, all calculations are carried out on identical grids and using the same numerical method, which is also the method employed by Sotiropoulos and Patel[6] with the LSH closure. For the k-ε model the two-point wall-function procedure of Patel et al.[9] is adopted. For the GL closure, however, this procedure is generalized to a three-point wall-function approach. Such an approach facilitates the calculation of all six Reynolds stresses at the node adjacent to the wall from the algebraic version of the GL closure.

In what follows, we first review previous attempts to calculate the flow through the CR duct of Davis and Gessner.[5] This is followed by brief descriptions of the two turbulence models, the three-point wall-function procedure in generalized curvilinear coordinates and the numerical method. Subsequently, extensive comparisons of the computed solutions with experimental data and with the previous near-wall calculations of Sotiropoulos and Patel[6] are presented and discussed. Finally, the calculations of Sotiropoulos and Patel[6] are also employed to evaluate the various terms in the vorticity transport equation (1) to further analyze the relative importance of the Reynolds stresses in the origin and evolution of longitudinal vorticity.

Previous Results for Flow in a Transition Duct

Davis and Gessner[5] reported very detailed turbulent flow measurements (all three mean-velocity components and all six Reynolds stresses) for a CR transition duct. The flow in the transition section is affected by the change in the cross-sectional shape and the associated wall curvatures, both longitudinal and transverse, by the initial diffusion and subsequent contraction due to change in area and by the pressure gradients associated with these rapid changes. The data of Davis and Gessner[5] show that these factors together induce a strong secondary motion which significantly distorts the streamwise mean-velocity and Reynolds stress fields.

In a recent study, Sotiropoulos and Patel[6] employed the near-wall, Reynolds stress transport closure of Launder and Shima[7] to calculate the flow through the CR duct. Their calculations were very successful in reproducing most of the experimentally observed features within the transition region; in particular, the origin and growth of longitudinal vorticity and its interaction with the mean streamwise flow and Reynolds-stresses were resolved with remarkable accuracy. Discrepancies in the agreement between experiment and computations were observed, however, in the recovery region downstream of the end of the transition, where the computed Reynolds stress field appeared to relax toward equilibrium at a much faster than measured rate.

Calculations for the CR duct of Davis and Gessner[5] have been also reported by Sotiropoulos and Patel[10] using a two-layer k-ε model; by Demuren,[11] who employed the standard k-ε model and a full Reynolds-stress transport closure, both with wall functions; and more recently by Lien and Leschziner,[12] who employed several low-Reynolds number k-ε closures. The calculations by Sotiropoulos and Patel as well as those by Demuren failed to correctly capture the origin and growth of the secondary motion and, consequently, its effect on the streamwise velocity field. This is not surprising insofar as the two-layer k-ε predictions[10] are concerned because the inadequacy of the two-layer approach for complex vortical flows has already been established.[10] What is remarkable, however, is the very poor performance of the full Reynolds stress closure employed by Demuren,[11] particularly since it yielded results almost identical to those obtained by the standard k-ε model. In fact, the conclusions of Demuren's study appear to suggest that the successful predictions of Sotiropoulos and Patel[6] are exclusively due to the proper resolution of the near-wall flow rather than due to the non-isotropic closure they employed. Such a conclusion, however, can not be fully supported by the existing evidence since Demuren's calculations were not grid independent. Lien and Leschziner[12] attempted to clarify that issue, by carrying out fine-grid calculations using various low-Reynolds number k-ε models and arrived at conclusions very similar to Demuren's. More specifically, they argued that Reynolds-stress anisotropy plays a very minor role in the origin and growth of longitudinal vorticity within the transition region of the duct and, therefore, an isotropic model which properly resolves the near wall layers should suffice for successful predictions. Their results, however, do not appear to support such a conclusion. Although their calculations produced a clearly defined vortex pair at the end of the transition region, the magnitude of the calculated secondary flow vectors in the vicinity of the vortex core appears to be up to 50% smaller than indicated by the data of Davis and Gessner. Furthermore, at the end of the transition region and in the vicinity of the vortex pair the streamwise velocity is overpredicted by approximately 18% and there is a substantial underprediction (by about 33%) of the peak value of the turbulence kinetic energy, both of which are clear signs of poor resolution of the secondary motion.

The work reported here was undertaken to resolve the various issues raised by these previous studies. More specifically, it is intended to clarify the relative roles of near-wall modeling and stress anisotropy on the prediction of the secondary motion.

Turbulence Models

As already indicated, two high-Reynolds number closures are employed: 1) the standard k-ε model and 2) the Reynolds stress transport closure of Gibson and Launder.[8] The governing equations of both closures are formulated in generalized, nonorthogonal, curvilinear coordinates. Because of space considerations and since these equations have already been published elsewhere, the reader is referred to Sotiropoulos and Patel[6,10] for the complete form of the curvilinear coordinate version of the k-ε and Reynolds stress transport equations, respectively. It is important to emphasize here, however, that the constants in the k-ε model assume their standard values: $C_\mu = 0.09$, $C_{\varepsilon 1} = 1.44$, $C_{\varepsilon 2} = 1.92$, $\sigma_k = 1.0$, and $\sigma_\varepsilon = 1.3$. Also, the GL closure employed here differs from the LSH closure described in Sotiropoulos and Patel[6] in two respects. First, the C_1, C_2, C_1^w, and C_2^w coefficients that appear in the model for the pressure-strain correlation are constant, rather than being functions of the anisotropy tensor as in the LSH closure.[7] More specifically, their values are those proposed by Gibson and Launder[8]: $C_1 = 1.8$, $C_2 = 0.6$, $C_1^w = 0.5$, and $C_2^w = 0.3$. Second, the ε equation in

the GL closure is the standard high-Reynolds number version also employed in the k-ε model.

In the k-ε model the Reynolds stresses that appear in the Reynolds averaged Navier–Stokes equations are related to the mean flow via an isotropic eddy viscosity. Obviously, this is not necessary when the GL closure is employed since the solution yields the individual stresses.

Numerical Method

The numerical method of Sotiropoulos and Patel[6,10,13] is used in the present study. This method solves the Reynolds averaged Navier–Stokes equations, in conjunction with either two-equation or full Reynolds stress closures, in generalized curvilinear coordinates. These equations are discretized on a nonstaggered (regular) computational grid using: 1) second-order accurate central finite-difference approximations for the divergence operator in the continuity equation and the pressure gradient and viscous terms in the momentum equations and 2) second-order accurate upwind differencing for the convective terms in the momentum equations. The incompressibility constraint is enforced through a discrete pressure-Poisson equation, designed to eliminate the problems associated with the use of a nonstaggered computational grid. The discrete momentum and turbulence closure equations are integrated in time using the four-stage explicit Runge-Kutta scheme enhanced with convergence-acceleration techniques such as local time stepping and implicit residual smoothing. The pressure equation is solved using the alternate direction implicit (ADI) method. More details about the numerical methodology can be found in Sotiropoulos and Patel.[6,10,13]

Test Case and Computational Details

A sketch of the CR transition duct along with the curvilinear coordinate system and locations of the measurement sections are shown in Fig. 1. The computational domain extends from section 1 to section 6. The circular section at station 2 changes to a super-elliptic section, with an aspect ratio of 3.0, at station 5 over a transition length of 1.5 inlet diameters. In this transition region, the ratio of the local cross-sectional area to the inlet area increases from unity at station 2 to a maximum of 1.15 near the midpoint of transition before decreasing back to unity at station 5. At each streamwise location in the transition region, the cross-sectional shape is defined by the equation of a super ellipse. Between stations 1 and 2, as well as between stations 5 and 6, there is no change in the section shape and cross-sectional area. The details of the geometric definition of the CR transition duct can be found in Davis.[14]

Because of the symmetry of the duct and symmetric inlet-flow conditions, only one quadrant of the duct is simulated. A grid topology similar to that used by Sotiropoulos and Patel[6] is employed in the present study. Grid sensitivity tests indicated that a mesh with $71 \times 41 \times 41$ grid nodes in the axial, radial, and circumferential directions, respectively, is sufficient to obtain grid-independent solutions. As a result of the wall-function approach employed in the present study the first coordinate surface just off the solid wall is located, almost everywhere, at $n^+ = 70$, where $n^+ = u_\tau n/\nu$, n is the normal distance from the wall and u_τ is the friction velocity, with 10 points within $70 < n^+ < 120$ (see subsequent section for details). All calculations are carried out at a Reynolds number, $Re = 3.9 \times 10^5$, based on the bulk velocity and inlet diameter.

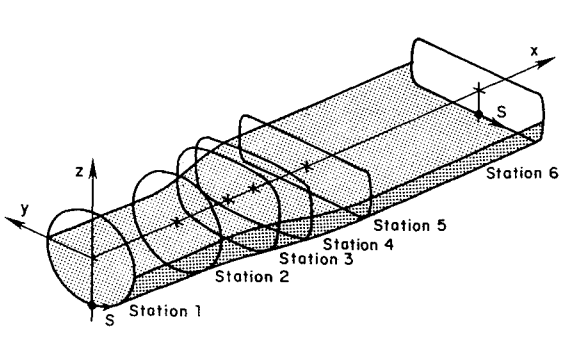

Fig. 1 Coordinates and locations of measurement stations for the CR transition duct of Davis and Gessner.

Boundary Conditions

Inlet conditions at section 1 are specified using the data of Davis and Gessner,[5] who reported mean velocity measurements beyond the edge of the sublayer and Reynolds stress measurements for $y^+ > 200$. An in-depth discussion of the flow conditions at section 1 can be found in Davis.[14] Here it suffices to say that the inflow conditions correspond to developing pipe flow—with a boundary-layer thickness of approximately 14% of the inlet diameter and a friction coefficient of 0.0033—and that the inlet profiles for the mean velocity and turbulence statistics were set up in an identical manner as in Sotiropoulos and Patel.[6]

On the symmetry boundaries, the governing equations are solved in exactly the same way as for every internal computational node using mirror-image reflection for the grid and the flow variables. At the exit boundary (section 6) all flow variables are computed by assuming zero streamwise diffusion.

Wall functions are used in both the k-ε and GL closure to bridge the gap between the logarithmic layer and the wall. For the k-ε calculations, the two-point wall function approach of Patel et al.[9] is employed. This approach avoids the need for separate analysis of the flow between the wall and the first near-wall mesh point which is used in the standard wall functions.[15] The details of the implementation of the two-point wall function in generalized curvilinear coordinates can be found in Patel et al.[9]; the only difference between the present implementation and that of Patel et al. is that the standard logarithmic law of the wall is employed herein in place of the generalized law of the wall of Patel.[16]

The GL closure requires boundary conditions for all six Reynolds stresses. For that reason, the two-point wall-functions approach is extended to a three-point procedure which allows determination of all six stresses from the algebraic version of the GL closure. A brief description of the procedure is given next.

To facilitate the description of the three-point wall-function procedure, assume that the wall is located at $\zeta = 0$. When constructing the computational mesh we ensure that the three near-wall coordinate surfaces $\zeta = 1$, 2, and 3 are located within the fully turbulent region (typically in the range $70 < n^+ < 100$). Starting now from an appropriate initial guess, the momentum, Reynolds stress, and ε equations are advanced to the next time level up to the $\zeta = 3$ surface. The magnitude of the computed velocity vector at $\zeta = 3$ is then used in conjunction with the logarithmic law of the wall to obtain the friction velocity u_τ; the resulting nonlinear equation is solved with the Newton-Raphson method. With u_τ known, the law of the wall is once again employed to obtain the magnitude of the velocity vectors at $\zeta = 1$ and 2. The three Cartesian velocity components at $\zeta = 1$ and 2 can then be computed by 1) assuming that the flow is parallel to the wall and 2) obtaining the angle between the streamwise coordinate and the projection of the velocity vector on the wall via extrapolation from the interior nodes (see Patel et al.[9] for details). The velocity components at $\zeta = 2$ serve as boundary conditions for the momentum equations, whereas those at $\zeta = 1$ are used to discretize, at $\zeta = 2$, the velocity gradient terms in the production and pressure-strain tensors that appear in the modeled Reynolds stress equations. The Reynolds stresses at $\zeta = 2$, necessary for computing the Reynolds stress gradients in the momentum equations and for providing boundary conditions for the Reynolds stress transport equations at $\zeta = 3$, are obtained in accordance with a local equilibrium assumption by setting all transport terms in the GL closure equal to zero and solving the resulting system of algebraic equations. The energy dissipation at $\zeta = 2$ is obtained by setting it equal to the production of turbulence kinetic energy.

Results and Discussion

In this section, the solutions obtained with the k-ε and GL closures are compared with each other, the measurements of Davis and Gessner,[5] and the LSH calculations of Sotiropoulos and Patel.[6] Comparisons include wall-pressure coefficient and skin-friction distributions, near-wall velocity and Reynolds-stress profiles, mean longitudinal velocity and vorticity contours, and turbulence kinetic

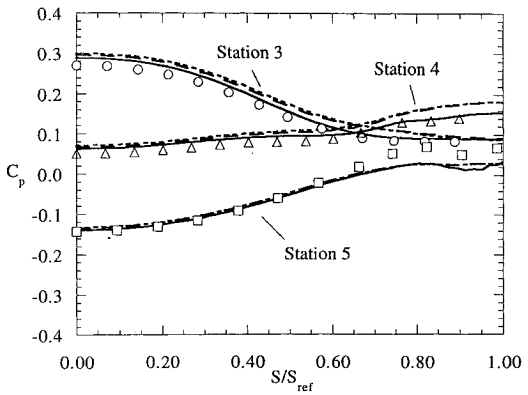

Fig. 2 Peripheral pressure coefficient distributions, $C_p = 2(P-P_0)/(\rho U_b^2)$: symbols experiment of Davis and Gessner, continuous line LSH, long dash GL, and short dash k-ε.

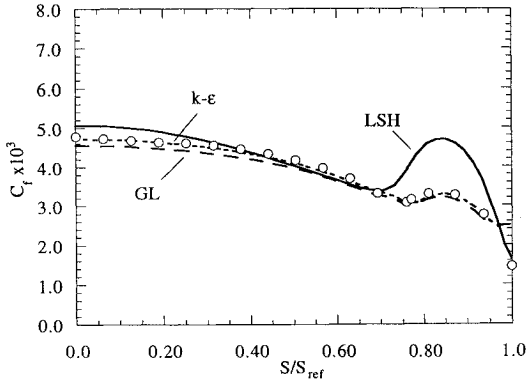

Fig. 3 Peripheral skin friction distribution at station 5: symbols experiment of Davis and Gessner, continuous line LSH, long dash GL, and short dash k-ε.

energy contours. Also, the LSH solution is used to evaluate the various terms in the transport equation for the mean longitudinal-vorticity equation (1). The relative magnitudes of the various terms are analyzed and their implications are discussed.

Since the main objective of the present study is to examine the role of turbulence anisotropy and near-wall modeling in predicting the origin and growth of longitudinal vorticity, the various comparisons are restricted to the three sections within the transition region, namely, stations 3, 4, and 5 shown in Fig. 1.

In the presentation of the results, all quantities are made dimensionless using the bulk velocity U_b and duct inlet radius R as the normalizing scales, along with the fluid properties, as appropriate. In the presentation and discussion of the flow in the near-wall region, however, the usual wall coordinates based on the local value of the friction velocity u_τ are used. The mean-velocity components in the (x, y, z) coordinates shown in Fig. 1 are denoted by (U, V, W) and the corresponding turbulent fluctuations by (u, v, w).

Pressure Distributions

The circumferential distributions of measured and computed wall static pressure coefficient at stations 3, 4, and 5 are shown in Fig. 2. Here, S is the distance around the perimeter measured from the center of the longer (bottom or horizontal) wall, and S_{ref} is one quarter of the local total cross-sectional perimeter. It seen that all three closures predict the wall-pressure distribution reasonably well, with the LSH[6] predictions being in somewhat better agreement with the measurements. In particular at station 3, and between $0.55 < S/S_{ref} < 0.8$, the LSH[6] closure yields, in agreement with the measurements, a steeper, as compared to the GL and k-ε predictions, negative pressure gradient ($\partial P/\partial S < 0$); note that it is this negative pressure gradient that drives the secondary motion along the duct wall from the vertical to the horizontal plane of symmetry and eventually leads to the formation of a pair of longitudinal vortices. Overall, however, the three predictions are quite similar, so that it appears unlikely that the subsequently discussed discrepancies in the prediction of the mean flow are due to insufficient resolution of the pressure field.

Wall Shear-Stress Distributions

The computed circumferential distributions of the wall shear-stress coefficient C_f at station 5 are compared with measurements in Fig. 3. All three closures yield very similar friction distributions along the horizontal wall, but significant discrepancies are observed along the vertical wall ($S/S_{ref} > 0.65$) where a longitudinal vortex pair forms and is responsible for the local maximum in the measured friction. The k-ε and GL closures reproduce almost all of the measured trends with remarkable accuracy, the only exception being the overprediction of the wall shear stress at the horizontal plane of symmetry ($S/S_{ref} = 1.0$). The LSH closure[6] appears to grossly overpredict the friction distribution in the region $0.7 < S/S_{ref} < 0.95$, which is along the vertical wall of the duct. This spectacular discrepancy is rather surprising and requires further analysis.

First, it is important to point out that Davis and Gessner[5] deduced C_f from Preston tubes, a technique that relies on the near-wall velocity distribution to obey the standard law of the wall, $u^+ = F(n^+)$, which is logarithmic, $u^+ = \kappa^{-1} \ell_n(n^+) + B$, with $\kappa = 0.42$ and $B = 5.45$, beyond the sublayer and the buffer layer. The wall functions used in the GL and k-ε closures rely on the same assumption and, particularly, on the logarithmic law. Therefore, the close agreement between the measured and calculated C_f should be regarded as agreement with respect to the velocity profile shape in the wall region but not a confirmation of the existence of the law of the wall. In particular, such a comparison does not validate or refute the existence of the law of the wall in this three-dimensional flow, because that would require an independent method of measuring C_f.

In the LSH calculations, C_f is determined directly from the slope of the velocity profile at the wall, and it appears that the disagreement between the LSH results and others shown in Fig. 3 is related to the breakdown of the usual logarithmic law and, therefore, the wall-functions approach in the region $0.7 < S/S_{ref} < 0.95$. To investigate this possibility, the results of the LSH calculations were reanalyzed in two different ways. First, C_f was re-evaluated by fitting the logarithmic law to the calculated velocity profile. Figure 4 shows the results, on an expanded scale. It is clear that the resulting values, labeled LSH1, are in close agreement with the measured values, as were the other calculations using wall functions, shown in Fig. 3.

The second reanalysis of the LSH calculations involves making a correction for the favorable pressure gradient that is present in this region of the transition duct. This is done by fitting the calculated velocity profiles to the extended law of the wall due to Patel[16]

$$u^+ = \frac{1}{\kappa}\left\{ \ell_n\left[\frac{4}{\Delta_\tau}\frac{(1+\Delta_\tau n^+)^{\frac{1}{2}}-1}{(1+\Delta_\tau n^+)^{\frac{1}{2}}+1}\right] + 2\left[(1+\Delta_\tau n^+)^{\frac{1}{2}}-1\right]\right\} + B + 3.7\Delta_p \qquad (2)$$

where $u^+ = q/u_\tau$, q is the magnitude of the velocity vector, $\Delta_p \equiv (u_\tau^3/Re)\nabla p$ is the dimensionless pressure gradient parameter, and Δ_τ is the dimensionless shear-stress gradient parameter which is set equal to Δ_p. Equation (2) is plotted in Fig. 5 for various values of Δ_p; note that $\Delta_p = 0$ corresponds to the standard law of the wall whereas $\Delta_p < 0$ corresponds to favorable pressure gradients. The resulting values of C_f are also shown in Fig. 4, labeled LSH2. It is seen that a correction for only the effect of pressure gradients is sufficient to bring the recalculated C_f closer to that predicted directly from the profile slope at the wall, labeled LSH. Perfect agreement between LSH2 and LSH would not be expected because Eq. (2) is no more than a model, and it does not account for the effects of three dimensionality which are undoubtedly present.

It is important to stress that neither LSH1 nor LSH2 involves a separate solution. They are the results of using the standard and an extended law of the wall to deduce C_f. The results presented in Fig. 4 lead to the conclusion that the LSH prediction is not in error. Rather, it is the use of the standard law of the wall, in Preston tubes

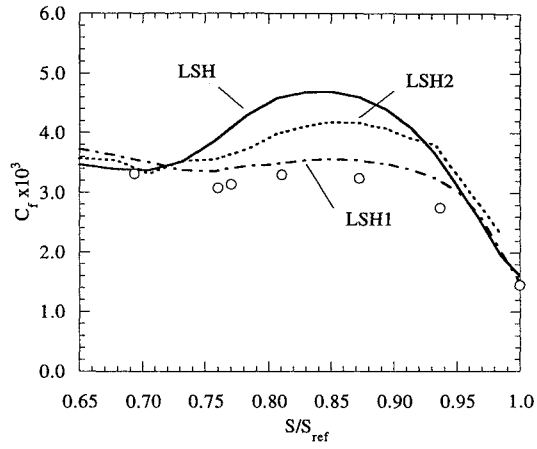

Fig. 4 Skin friction distribution along the vertical wall at station 5: symbols experiment of Davis and Gessner, continuous line LSH, dash-dot LSH1, and short dash LSH2.

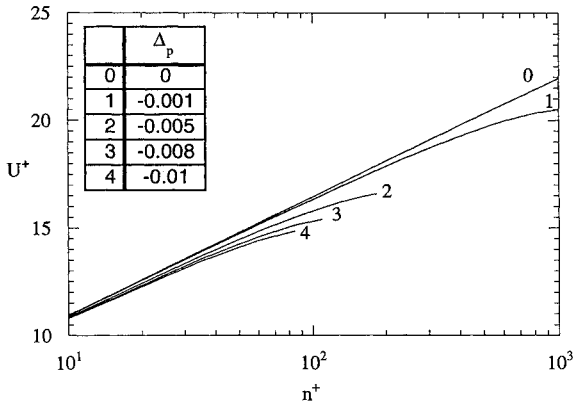

Fig. 5 Influence of pressure gradient on the law of the wall; plot of Eq. (2) for zero and favorable pressure gradient.

as well in the wall functions, that leads to the agreements shown in Fig. 3.

Mean Velocity, Longitudinal Vorticity and Turbulence Kinetic Energy Distributions

Figure 6 shows the measured and calculated contours of the streamwise component of mean velocity at station 5. The measurements exhibit a region of low velocity located near the junction between the horizontal plane of symmetry and the vertical wall. This is associated with a longitudinal vortex pair (see Fig. 7) that forms as a result of the secondary motion. These vortices, with the common flow between them directed away from the side wall, transport low velocity fluid from the wall boundary layers toward the center of the cross section. The k-ε prediction fails to predict the distorted shapes of the measured isovels in the vicinity of the vortex pair; in fact, the calculated velocity contours do not exhibit any distortion at all. The GL closure, on the other hand, produces only a mild distortion of the velocity contours, whereas the LSH closure[6] reproduces the measurements of Davis and Gessner with remarkable accuracy. These differences in the prediction of the streamwise velocity distribution should correlate with the ability of each closure to resolve the origin and growth of the secondary motion. One can speculate, for instance, that the k-ε closure predicts a secondary motion so weak that no longitudinal vortex forms, whereas the GL closure yields a longitudinal vortex which is too weak to fully interact with the streamwise flow.

The secondary motion is best visualized through contours of the mean longitudinal vorticity ($\Omega_x R/U_b$) constructed by differentiation of the transverse mean-velocity components (V and W). The experimental and computed contours at station 5 are shown in Fig. 7. In this figure, the sign of the experimental vorticity contours, which changes across planes of symmetry, has been reversed to facilitate

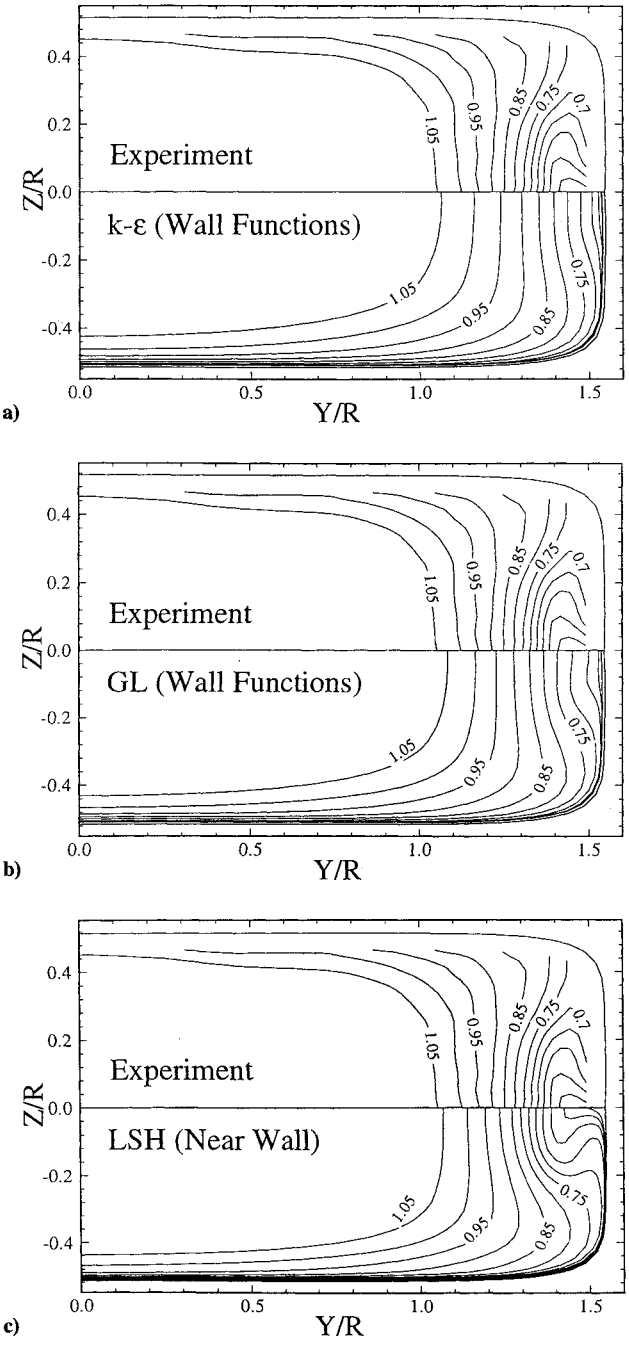

Fig. 6 Measured (Davis and Gessner) and computed contours of mean streamwise velocity (U/U_b) at station 5.

comparisons with the calculations. As anticipated from the predictions of the streamwise velocity, the secondary motion calculated by the k-ε closure does not lead to a distinct longitudinal vortex whereas the GL closure predicts a well-defined, although much weaker than measured, vortex. More specifically, the GL closure predicts a core vorticity value of about 1.1 which is about 50% smaller than that measured by Davis and Gessner.[5] Furthermore, the location of the calculated vortex does not correspond to that indicated by the measurements, the calculated vortex being closer to the vertical wall and farther away from the horizontal symmetry plane. Despite the failure of both closures (k-ε and GL) to reproduce the measured vorticity field, the fact that the GL closure produces a distinct longitudinal vortex indicates that the Reynolds stress terms in the vorticity transport equation [Eq. (1)] have become significant at the end of the transition region. This conclusion contradicts the preliminary findings, pending further grid refinement studies, of Demuren[11] who calculated the same flow using the standard k-ε model and a Reynolds stress transport model, both in conjunction

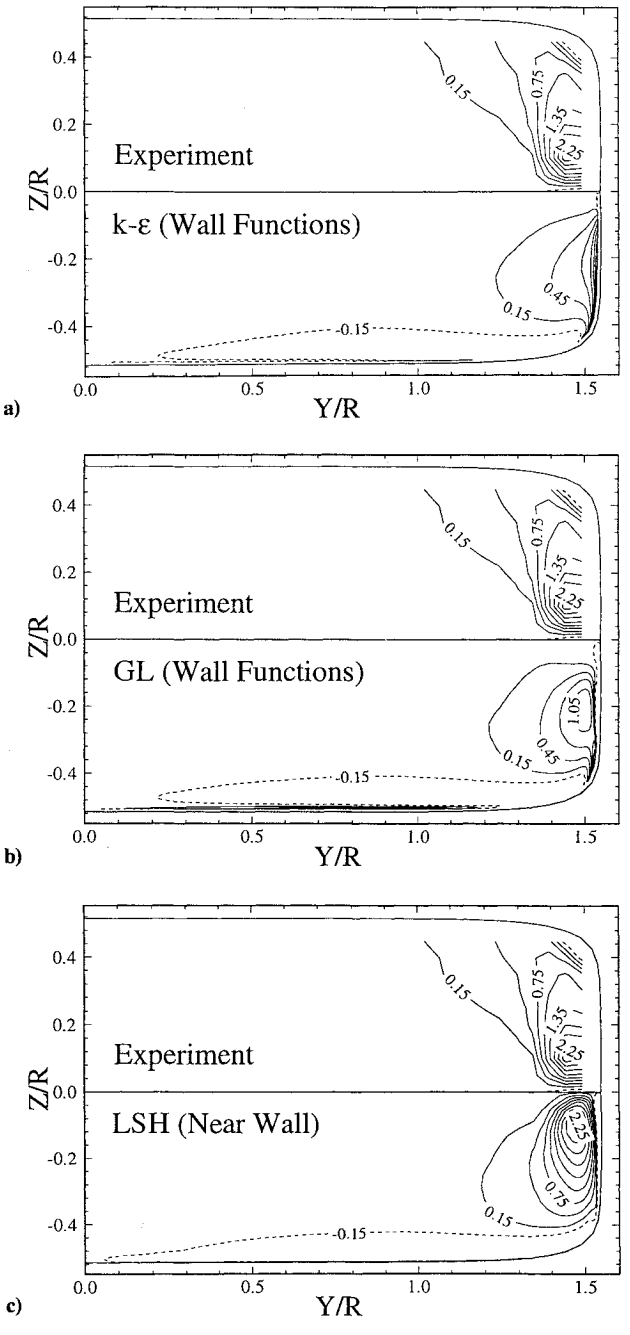

Fig. 7 Measured (Davis and Gessner) and computed contours of mean longitudinal velocity ($\Omega_x R/U_b$) at station 5.

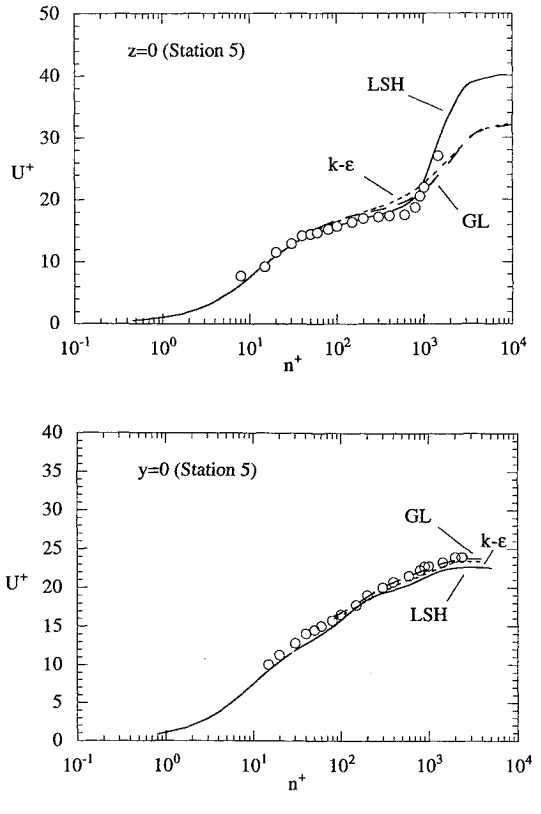

Fig. 8 Mean velocity profiles in wall coordinates in the symmetry planes at station 5: symbols experiment of Davis and Gessner, continuous line LSH, long dash GL, and short dash k-ε.

with wall functions, and reported very little difference between the two turbulence models; both closures failed to predict a longitudinal vortex. That led Demuren[11] to conclude that turbulence-induced secondary motion had not become significant at the end of the transition region. However, the present results along with the subsequent discussion of the budget for the mean longitudinal vorticity suggest otherwise. Furthermore, from comparison of the k-ε and GL predictions with the very successful LSH predictions, also shown in Fig. 7, it becomes clear that the wall-functions approach, whether it is used in isotropic or nonisotropic closures, is inadequate to resolve complex three-dimensional flows. It is important to emphasize, that all calculations in the present study have been carried out with the same numerical method, on grids of similar size, and have undergone grid dependency studies, so that any numerical uncertainties have been carefully minimized.

Figure 8 depicts the measured and computed mean velocity profiles plotted in wall coordinates along the horizontal ($z = 0$) and vertical ($y = 0$) planes of symmetry at section 5. These plots clearly demonstrate the successful implementation of the two- and three-point wall function approaches employed with the k-ε and GL closures, respectively. Along the horizontal plane of symmetry (Fig. 8a) the data exhibit a small logarithmic region up to $n^+ = 80$; beyond this, and up to about $n^+ > 1000$, they lie below the logarithmic line due to the favorable longitudinal pressure gradient that is present. Farther from the wall, for $n^+ < 1000$, the region of very large velocity gradients is associated with the longitudinal vortex structure. Only the LSH closure correctly predicts all of the experimental trends. The k-ε and GL closures respond correctly to the pressure gradient but yield a milder than measured velocity gradient in the outer layer, a trend which is consistent with the underestimation of the secondary motion. Along the vertical plane of symmetry (Fig. 8b), all three closures yield very similar velocity profiles, with the LSH prediction lying somewhat below the measurements, a trend consistent with the slightly higher predicted C_f at $S = 0$ (see Fig. 3).

Figure 9 shows the measured and computed contours of turbulence kinetic energy at station 5. Both the GL and LSH closures capture the pocket of high turbulence kinetic energy exhibited by the measurements in the vicinity of the horizontal plane of symmetry. In the GL prediction, however, this pocket is located closer than indicated by the measurements to the horizontal wall and does not exhibit the distortion of the measured k contours. The k-ε closure, on the other hand, does not produce a distinct pocket of increased turbulence intensity, and it yields excessive values of k everywhere along the horizontal and vertical walls.

In Figs. 10 and 11 the measured and computed, by the GL and LSH closures, profiles of the three normal Reynolds stresses and the primary shear stress are plotted in wall coordinates along the horizontal (Fig. 10) and vertical (Fig. 11) planes of symmetry at station 5. In these figures, $(\overline{u^2})^+$, $(\overline{v^2})^+$, $(\overline{w^2})^+$, $(\overline{uv})^+$, and $(\overline{uw})^+$, denote $\overline{u^2}/u_\tau^2$, $\overline{v^2}/u_\tau^2$, $\overline{w^2}/u_\tau^2$, $-\overline{uv}/u_\tau^2$, and $-\overline{uw}/u_\tau^2$, respectively. With the only exception the overprediction of the axial normal stress by GL closure, both closures yield similar results along the vertical plane of symmetry (Fig. 11) where the flow exhibits boundary-layer characteristics. As expected from the previously presented turbulence kinetic energy contours (Fig. 9), however, there are significant differences between the two predictions along the horizontal

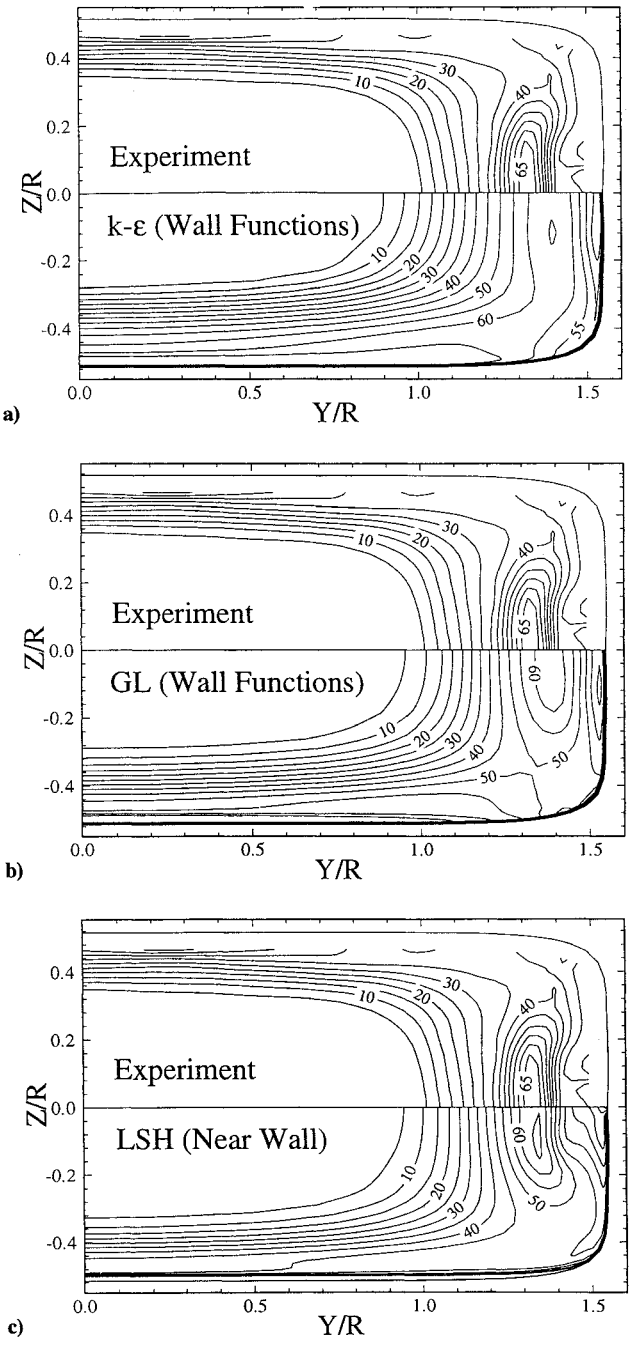

Fig. 9 Measured (Davis and Gessner) and computed contours of turbulence kinetic energy ($k/U_b^2 \times 10^4$) at station 5.

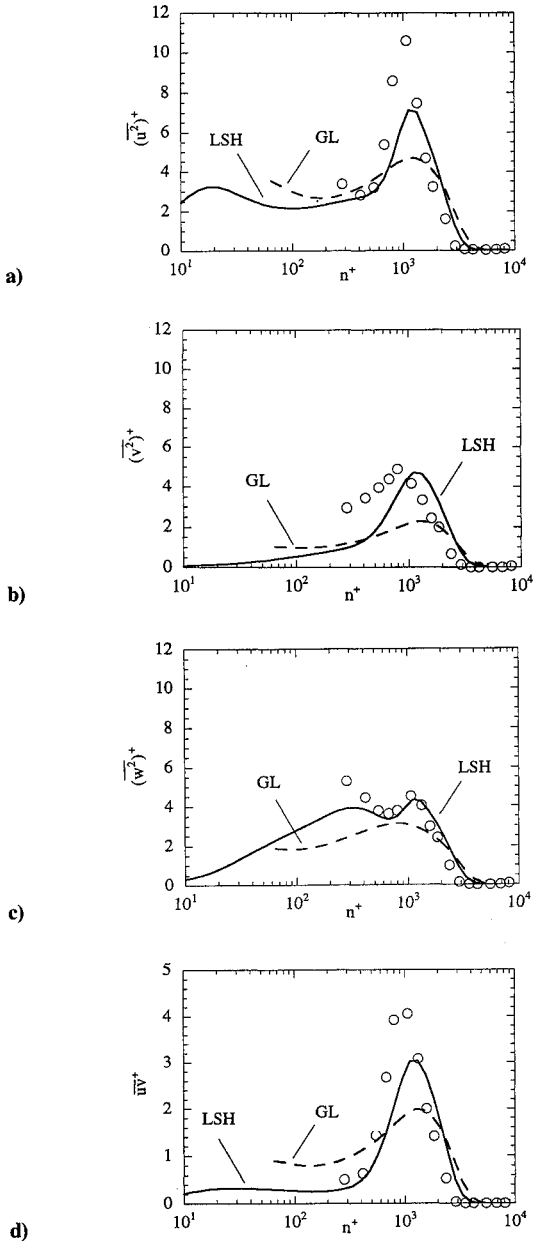

Fig. 10 Reynolds stress profiles in wall coordinates along $z = 0$ at station 5: symbols experiment of Davis and Gessner, continuous line LSH, and long dash GL.

plane of symmetry (Fig. 10). The LSH closure, for instance, captures both qualitatively and quantitatively almost all experimental trends. The GL closure, on the other hand, underpredicts the levels of all Reynolds stresses in the vicinity of $n^+ = 1000$, which corresponds to the pocket of increased turbulence intensity observed in Fig. 9, and does not capture the two peaks observed in the measured distribution of $(\overline{w^2})^+$. A particularly important feature, regarding the performance of the two closures in the logarithmic region, is the failure of the GL closure to predict correctly both the levels and the gradients of the Reynolds stresses near $n^+ = 70$, where the wall-functions boundary conditions are applied. This failure further demonstrates the inadequacy of the wall-functions approach, and the local equilibrium assumptions associated with it, for simulating complex, nonequilibrium, shear flows.

Longitudinal Vorticity Budget

In this section the LSH solution[6] is employed to calculate the various terms in the transport equation for mean longitudinal vorticity. These terms are evaluated numerically by finite differencing the computed mean-velocity and Reynolds stress fields. For that reason, Eq. (1) is first transformed to generalized curvilinear coordinates, and the various terms in it are computed at various sections within the transition region using three-point central (second-order accurate) finite-difference formulas. For the following discussion, these terms are nondimensionalized in the manner stated earlier (i.e., the values quoted are those of A_2R^2/U_b^2, etc.). Furthermore, the A_4 term in Eq. (1) is divided into two parts, one containing all spatial derivatives of the shear stresses and the other containing the remaining transverse normal-stress anisotropy term. Each one of these terms is plotted separately, in all subsequently presented figures, to investigate its relative importance in producing and diffusing longitudinal vorticity. Care should be exercised, however, when interpreting the physical significance of these terms as they are expressed in Cartesian coordinates. Therefore, only beyond station 5, where the cross-sectional shape is almost rectangular, the shear-stress and normal-stress anisotropy terms assume fully the physical meaning implied by their corresponding names.

Contour plots of the calculated values of the various terms in Eq. (1) are shown in Figs. 12–14 for sections 3–5 along the duct.

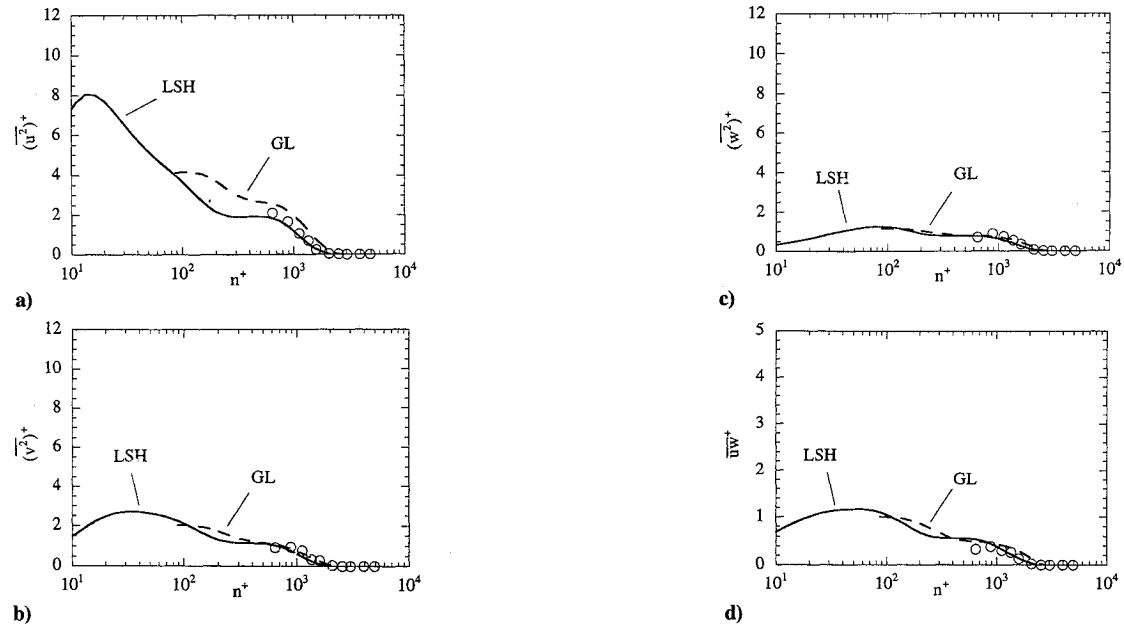

Fig. 11 Reynolds stress profiles in wall coordinates along $y = 0$ at station 5: symbols experiment of Davis and Gessner, continuous line LSH, and long dash GL.

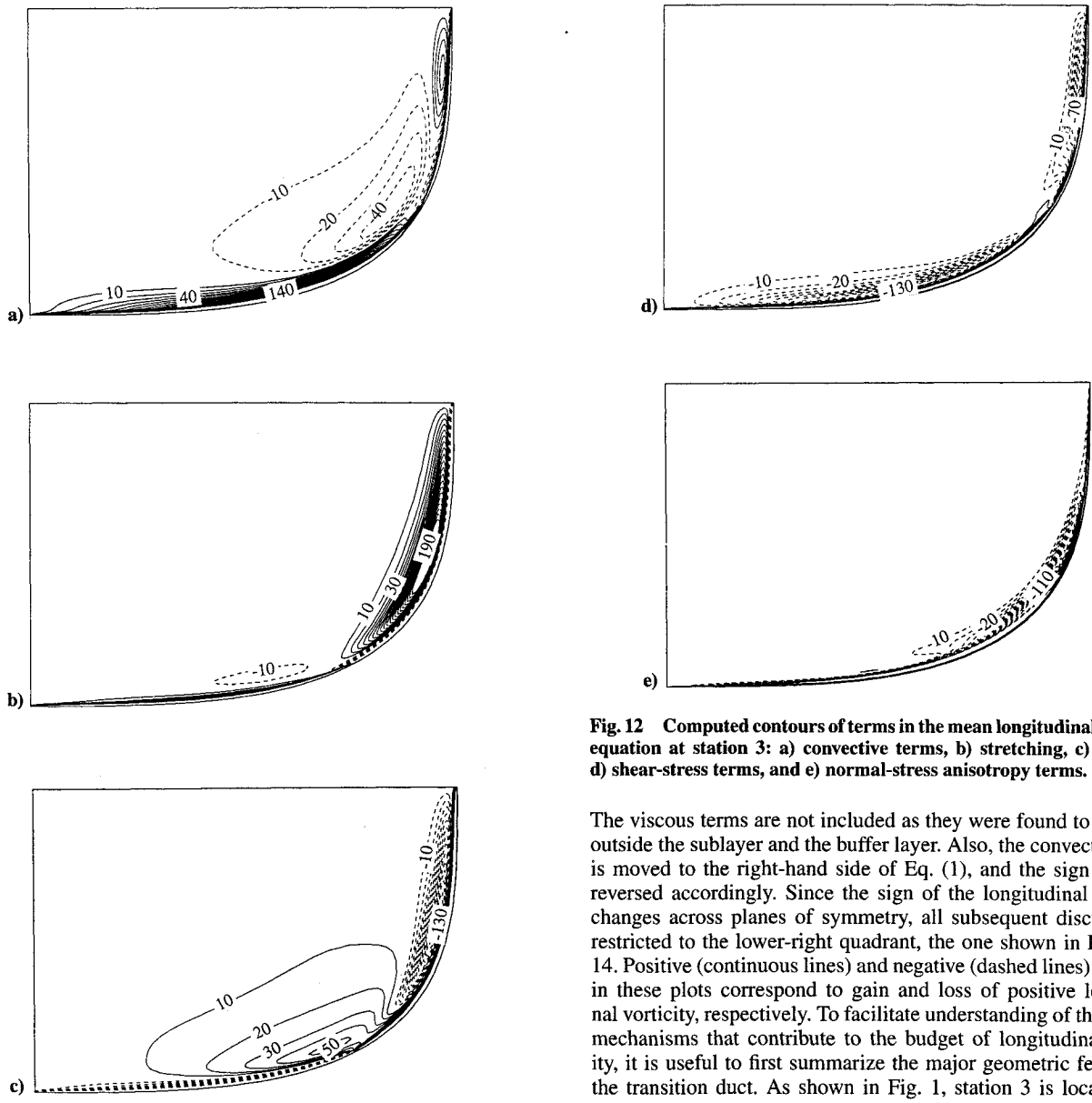

Fig. 12 Computed contours of terms in the mean longitudinal vorticity equation at station 3: a) convective terms, b) stretching, c) skewing, d) shear-stress terms, and e) normal-stress anisotropy terms.

The viscous terms are not included as they were found to be small outside the sublayer and the buffer layer. Also, the convection term is moved to the right-hand side of Eq. (1), and the sign of A_1 is reversed accordingly. Since the sign of the longitudinal vorticity changes across planes of symmetry, all subsequent discussion is restricted to the lower-right quadrant, the one shown in Figs. 12–14. Positive (continuous lines) and negative (dashed lines) contours in these plots correspond to gain and loss of positive longitudinal vorticity, respectively. To facilitate understanding of the various mechanisms that contribute to the budget of longitudinal vorticity, it is useful to first summarize the major geometric features of the transition duct. As shown in Fig. 1, station 3 is located very

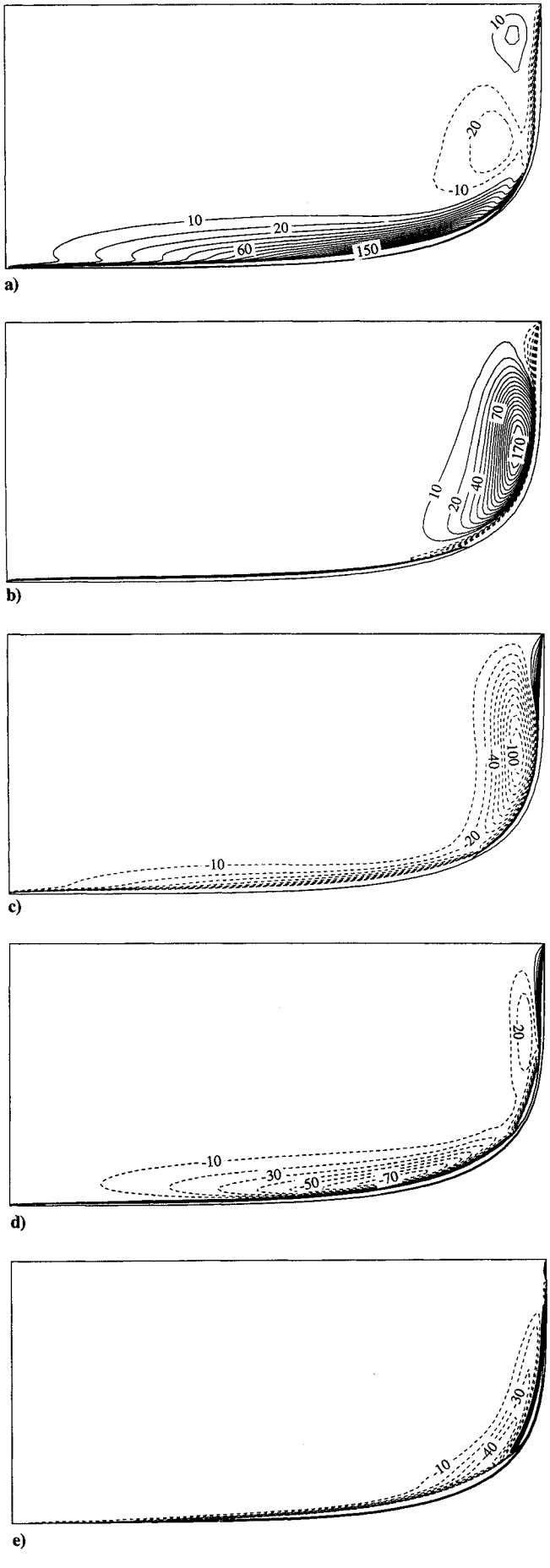

Fig. 13 Computed contours of terms in the mean longitudinal vorticity equation at station 4: a) convective terms, b) stretching, c) skewing, d) shear-stress terms, and e) normal-stress anisotropy terms.

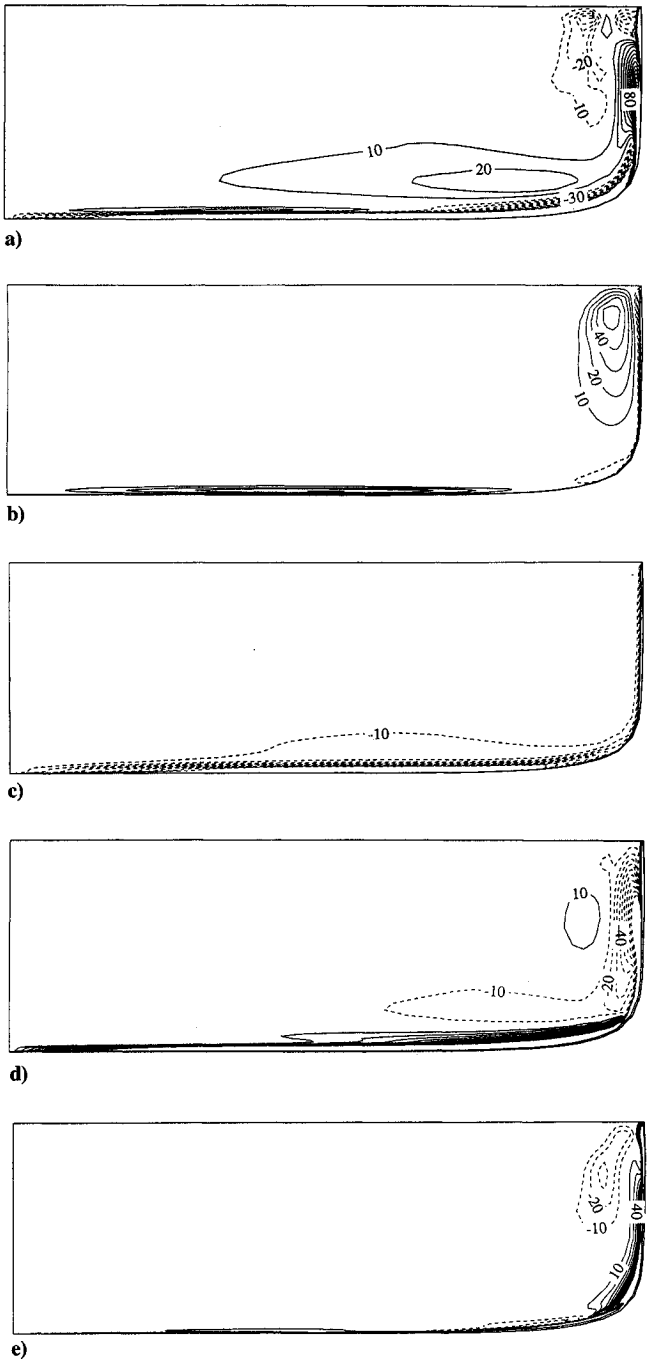

Fig. 14 Computed contours of terms in the mean longitudinal vorticity equation at station 5: a) convective terms, b) stretching, c) skewing, d) shear-stress terms, and e) normal-stress anisotropy terms.

near the midpoint of transition where the area expansion is almost completed. The area at this station is 14.7% larger than that at station 2, whereas the overall area increase is 15%. Station 3, on the other hand, is located in the second-half of transition where the area contraction takes place (the cross-sectional area is 10.87% larger than that at station 2). Stations 5 and 6 are located at the end of the transition and the end of the straight recovery region, respectively. The cross-sectional area at both stations is equal to the inlet area.

From the results at section 3 shown in Fig. 12 it is clear that all terms in the longitudinal vorticity equation are comparable in magnitude in this cross section as a whole, but each is predominant in some part of the section. The negative circumferential pressure gradient in this section (see Fig. 2) induces a secondary motion from the bottom to the side wall. This results in a region of intense production of longitudinal vorticity by lateral skewing near the corner region

(Fig. 12c). In the vicinity of the side wall, the sign of the skewing term (A_3) is reversed, and it acts to produce negative longitudinal vorticity. This region of negative skewing is balanced, however, by a region of intense axial stretching (A_2 term), as seen in Fig. 12b, which tends to increase the positive longitudinal vorticity. Both the sign reversal of the skewing term and the triggering of the vortex stretching mechanism are due to the upstream influence of the area contraction that takes place downstream of section 3. The contraction in area induces a sign reversal of the transverse pressure gradient and streamwise acceleration of the mean flow. The Reynolds stress terms (A_4) also play an important role in balancing Eq. (1) at section 3. As seen from Figs. 12d and 12e, both the shear-stress and anisotropy terms work to decrease positive longitudinal vorticity everywhere along the wall. In fact, near the wall these terms are of the same order of magnitude as the stretching and skewing terms. The contours of the convective terms ($-A_1$), shown in Fig. 12a, indicate that there are two regions of net loss of longitudinal vorticity which are balanced by positive convection, namely, at the junction between the horizontal plane of symmetry and the side wall, where longitudinal vorticity is lost due to negative lateral skewing and stress-induced diffusion, and along the bottom wall, where stress-induced diffusion is the dominant mechanism. Finally, there is a large region of net gain of longitudinal vorticity which is balanced by negative convection. This region originates at the corner region due to the combined effects of stretching, skewing, and Reynolds stress terms.

At section 4 (Fig. 13), the sign of the circumferential pressure gradient is reversed (see Fig. 2), thus tending to cancel the positive longitudinal vorticity generated in the first-half of the transition duct. As a result, the lateral skewing terms are now negative throughout the cross section (with the exception of a thin region of positive skewing terms near the side wall), as seen in Fig. 13c, therefore, acting as a sink of positive longitudinal vorticity. At section 4, however, the flow experiences a global streamwise acceleration due to the area contraction.[14] As a result, the vortex stretching term (A_2) becomes the dominant mechanism, tending to counteract the effect of skewing by intensifying the positive longitudinal vorticity (see Fig. 13b). The Reynolds stress terms (Figs. 13d and 13e) continue to diffuse positive vorticity in the vicinity of the wall, with their magnitude increasing as the wall is approached. In fact, along the bottom wall, stress-induced diffusion is the dominant mechanism balanced only by positive convection. Moreover, a region of stress-induced production of vorticity has appeared near the side wall. The convective terms are negative near the side wall in order to balance the net increase of longitudinal vorticity by vortex stretching, whereas they are positive along the bottom wall to account for the stress-induced diffusion of vorticity. A small region of positive convection, which balances losses by negative skewing and stress-induced diffusion, is also observed near the junction between the side wall and the symmetry plane.

The longitudinal-vorticity budget at section 5, located at the end of the transition region, is shown in Fig. 14. In the vicinity of the side wall, the dominant terms in the longitudinal-vorticity equation are the stretching and Reynolds stress terms. More specifically, the vortex-stretching mechanism continues to intensify the positive vorticity but its magnitude is substantially reduced, since the area contraction is completed at the end of the transition region.[14] The shear-stress terms (Fig. 14d), on the other hand, act to reduce positive vorticity along the vertical endwall, with this trend reversing along the bottom wall. Perhaps the most remarkable feature at station 5, insofar as the role of the Reynolds stress terms is concerned, is the appearance of a region in the vicinity of the vortex core of fairly intense anisotropy-induced diffusion of vorticity (Fig. 14e). In fact, the anisotropy term in this region is of the same order as the vortex stretching term, a trend which underscores the significant role of turbulence anisotropy in the evolution of the longitudinal-vorticity field. The anisotropy term is also very important all along the vertical wall where, in contrast to the shear-stress terms, it acts to produce positive vorticity. Although there is no wall curvature at section 5, the lateral skewing terms (Fig. 14c) are still important near the bottom wall, acting as sink of positive vorticity; as already discussed (see Fig. 2), a significant positive circumferential pressure gradient still exists at the end of the transition region, and the secondary motion associated with it tends to cancel positive longitudinal vorticity. The positive sign of the convective terms along the bottom wall and close to the side wall indicates a net influx of positive vorticity to balance the losses due to stress-induced diffusion and negative lateral skewing. At the junction between the side wall and the plane of symmetry, however, negative convection marks the region of net increase of longitudinal vorticity due to vortex stretching.

It is evident from the results just described that both the Reynolds shear stress and anisotropy terms play an important role in the generation and destruction of longitudinal vorticity even within the transition region. Although longitudinal vorticity is initially generated by lateral skewing of the vorticity vector and subsequently intensified by vortex stretching in the axial direction, the Reynolds stress gradient terms in Eq. (1) make significant contributions by acting to decrease and, to a lesser extent generate, longitudinal vorticity throughout the transition region.

Summary and Conclusions

The standard k-ε model and the full Reynolds stress transport closure of Gibson and Launder, both with wall functions, were employed to calculate the flow through the circular-to-rectangular transition duct of Davis and Gessner. The computed solutions were compared with experimental data and with previously reported calculations which employed the near-wall Reynolds stress transport closure of Launder and Shima to investigate the importance of near-wall modeling and turbulence anisotropy in the prediction of the origin and growth of longitudinal vortices. The Launder and Shima solution was also employed to evaluate the terms in the transport equation for mean longitudinal vorticity in order to elucidate the importance of the various mechanisms responsible for the generation and evolution of secondary motion. This study leads to the following conclusions concerning computational modeling of three-dimensional flows.

1) The wall-functions approach, when used in either isotropic or second-moment closures, failed to capture the strength of the secondary motion and longitudinal vorticity in this three-dimensional flow in spite of the fact that two-point and three-point procedures were adopted to ensure compatibility and consistency with the parent turbulence models. This suggests that explicit modeling of the near-wall flow is needed to properly predict the secondary motion and longitudinal vorticity.

2) The results presented here suggest that friction coefficients deduced from the standard logarithmic law of the wall, whether by experiment or by calculations, may not be particularly meaningful due to the effects of pressure gradients, curvature, and three dimensionality in the near-wall flow on the law of the wall.

3) Evaluation of the various terms in the mean longitudinal-vorticity transport equation, in the transition duct, clearly demonstrated that vortex stretching, vortex skewing, and generation and destruction of vorticity by Reynolds stresses are all dominant in one region or the other. Thus, unlike conclusions reached in some recent studies, the present results clearly demonstrate that accurate description of most three-dimensional turbulent flows, regardless of their origin, would require near-wall turbulence closures that take into account the anisotropy of the Reynolds stresses.

Acknowledgments

This research was supported by the Office of Naval Research, Grant N00014-91-J-1204, monitored by L. P. Purtell. Tabulated experimental data were kindly provided by D. O. Davis. The calculations were carried out on the Cray X-MP/216 at the Idaho National Engineering Laboratories and the Cray C90 at the San Diego Supercomputer Center.

References

[1]Bradshaw, P., "Turbulent Secondary Flows," *Annual Review of Fluid Mechanics*, Vol. 19, 1987, pp. 53–74.

[2]Demuren, A. O., and Rodi, W., "Calculations of Turbulence-Driven Secondary Motion in Non-Circular Ducts," *Journal of Fluid Mechanics*, Vol. 140, 1984, pp. 189–222.

[3]Patel, V. C., Rodi, W., and Scheuerer, G., "Turbulence Models for Near-

Wall and Low-Reynolds Number Flows: A Review," *AIAA Journal*, Vol. 23, No. 9, 1985, pp. 1308–1319.

[4]So, R. M. C., Lai, Y. G., Zhang, H. S., and Hwang, B. C., "Second Order Near-Wall Turbulence Closures: A Review," *AIAA Journal*, Vol. 29, No. 11, 1991, p. 1819.

[5]Davis, D. O., and Gessner, F. B., "Experimental Investigation of Turbulent Flow Through a Circular-to-Rectangular Transition Duct," *AIAA Journal*, Vol. 30, No. 2, 1992, pp. 367–375.

[6]Sotiropoulos, F., and Patel, V. C., "Prediction of Turbulent Flow Through a Transition Duct Using a Second-Moment Closure," *AIAA Journal*, Vol. 32, No. 11, 1994, pp. 2194–2204.

[7]Launder, B. E., and Shima, N., "Second-Moment Closure for the Near-Wall Sublayer: Development and Application," *AIAA Journal*, Vol. 27, No. 10, 1989, pp. 1319–1325.

[8]Gibson, M. M., and Launder, B. E., "Ground Effects on Pressure Fluctuations in the Atmospheric Boundary Layer," *Journal of Fluid Mechanics*, Vol. 86, 1978, pp. 491–511.

[9]Patel, V. C., Chen, H. C., and Ju, S., "Solution of the Fully-Elliptic Reynolds-Averaged Navier-Stokes Equations and Comparisons with Experiments," Iowa Inst. of Hydraulic Research, IIHR Rept. 323, Univ. of Iowa, Iowa City, IA, 1988.

[10]Sotiropoulos, F., and Patel, V. C., "Flow in Curved Ducts of Varying Cross-Section," Iowa Inst. of Hydraulic Research, IIHR Rept. 358, Univ. of Iowa, Iowa City, IA, 1992.

[11]Demuren, A. O., "On the Generation of Secondary Motion in Circular-to-Rectangular Transition Ducts," AIAA Paper 93-0681, Jan. 1993.

[12]Lien, F. S., and Leschziner, M. A., "Modelling the Flow in a Transition Duct with a Non-Orthogonal FV Procedure and Low-Re Turbulence-Transport Models," *Advances in Computational Methods in Fluid Dynamics*, edited by K. N. Ghia, U. Ghia, and D. Goldstein, ASME FED-Vol. 196, American Society of Mechanical Engineers, Lake Tahoe, NV, 1994, pp. 93–106.

[13]Sotiropoulos, F., Kim, W. J., and Patel, V. C., "A Computational Comparison of Two Incompressible Navier-Stokes Solvers in Three-Dimensional Laminar Flows," *Computers and Fluids*, Vol. 23, No. 4, 1994, pp. 627–646.

[14]Davis, D. O., "Experimental Investigation of Turbulent Flow Through a Circular-to-Rectangular Transition Duct," Ph.D. Dissertation, Mechanical Engineering Dept., Univ. of Washington, WA, 1991.

[15]Launder, B. E., and Spalding, D. B., "The Numerical Computation of Turbulent Flow," *Computational Methods of Applied Mechanical Engineering*, Vol. 3, 1974, pp. 269–289.

[16]Patel, V. C., "A Unified View of the Law of the Wall Using Mixing-Length Theory," *Aeronautical Quarterly*, Vol. 24, 1973, pp. 55–70.